



ARL-TR-8501 • SEP 2018



# **Actuator Dynamics and Aeroelasticity for Canard Control on a Subsonic, Gun-Launched Munition**

**by Joshua T Bryson and Frank E Fresconi**

Approved for public release; distribution is unlimited.

## **NOTICES**

### **Disclaimers**

The findings in this report are not to be construed as an official Department of the Army position unless so designated by other authorized documents.

Citation of manufacturer's or trade names does not constitute an official endorsement or approval of the use thereof.

Destroy this report when it is no longer needed. Do not return it to the originator.



# **Actuator Dynamics and Aeroelasticity for Canard Control on a Subsonic, Gun-Launched Munition**

**by Joshua T Bryson and Frank E Fresconi**  
*Weapons and Materials Research Directorate, ARL*

REPORT DOCUMENTATION PAGE				Form Approved OMB No. 0704-0188	
<p>Public reporting burden for this collection of information is estimated to average 1 hour per response, including the time for reviewing instructions, searching existing data sources, gathering and maintaining the data needed, and completing and reviewing the collection information. Send comments regarding this burden estimate or any other aspect of this collection of information, including suggestions for reducing the burden, to Department of Defense, Washington Headquarters Services, Directorate for Information Operations and Reports (0704-0188), 1215 Jefferson Davis Highway, Suite 1204, Arlington, VA 22202-4302. Respondents should be aware that notwithstanding any other provision of law, no person shall be subject to any penalty for failing to comply with a collection of information if it does not display a currently valid OMB control number.</p> <p><b>PLEASE DO NOT RETURN YOUR FORM TO THE ABOVE ADDRESS.</b></p>					
1. REPORT DATE (DD-MM-YYYY) September 2018		2. REPORT TYPE Technical Report		3. DATES COVERED (From - To) February 2018–May 2018	
4. TITLE AND SUBTITLE Actuator Dynamics and Aeroelasticity for Canard Control on a Subsonic, Gun-Launched Munition				5a. CONTRACT NUMBER	
				5b. GRANT NUMBER	
				5c. PROGRAM ELEMENT NUMBER	
6. AUTHOR(S) Joshua T Bryson and Frank E Fresconi				5d. PROJECT NUMBER	
				5e. TASK NUMBER	
				5f. WORK UNIT NUMBER	
7. PERFORMING ORGANIZATION NAME(S) AND ADDRESS(ES) US Army Research Laboratory ATTN: RDRL-WML-E Aberdeen Proving Ground, MD 21005-5066				8. PERFORMING ORGANIZATION REPORT NUMBER  ARL-TR-8501	
9. SPONSORING/MONITORING AGENCY NAME(S) AND ADDRESS(ES)				10. SPONSOR/MONITOR'S ACRONYM(S)	
				11. SPONSOR/MONITOR'S REPORT NUMBER(S)	
12. DISTRIBUTION/AVAILABILITY STATEMENT Approved for public release; distribution is unlimited.					
13. SUPPLEMENTARY NOTES					
14. ABSTRACT <p>The US Army's modernization priority of long-range precision fires has identified a need for low-cost, high-g-survivable, fast-responding munition control actuation technologies. This research focuses on canard control actuation technologies for subsonic flight regimes. Munition flight simulations were performed to obtain flight characteristics encountered by the control actuators. Laboratory experiments were conducted to re-create the flight environment for the control actuation technology. Experimental results indicate that the transient response is not significantly degraded, to at least 3-Ncm canard hinge load (representative of Mach 0.6). However, the canard actuation assembly exhibits deformation that scales with the load. These static aeroelastic effects were quantified experimentally and assessed in Monte Carlo-guided flight simulations. Results suggest that static aeroelasticity does not affect delivery accuracy, which validates these specific technologies and the overall technical approach for achieving this mission.</p>					
15. SUBJECT TERMS <p>actuator dynamics and control, canard control actuation system, canard static aeroelasticity, coupled flight simulation, actuator flight load</p>					
16. SECURITY CLASSIFICATION OF:			17. LIMITATION OF ABSTRACT  UU	18. NUMBER OF PAGES  28	19a. NAME OF RESPONSIBLE PERSON Joshua T Bryson
a. REPORT Unclassified	b. ABSTRACT Unclassified	c. THIS PAGE Unclassified			19b. TELEPHONE NUMBER (Include area code) 410-306-1939

## **Contents**

---

<b>List of Figures</b>	<b>iv</b>
<b>List of Tables</b>	<b>v</b>
<b>1. Introduction</b>	<b>1</b>
<b>2. Airframe and Control Actuation</b>	<b>2</b>
<b>3. Actuator Dynamic Model</b>	<b>3</b>
<b>4. Canard Aerodynamic Model</b>	<b>4</b>
<b>5. Flight Conditions</b>	<b>5</b>
<b>6. Experimental Apparatus</b>	<b>7</b>
<b>7. Actuator Dynamic Response</b>	<b>9</b>
<b>8. Actuator Static Aeroelasticity</b>	<b>11</b>
<b>9. Coupled Flight Simulation Analysis</b>	<b>13</b>
<b>10. Conclusion</b>	<b>17</b>
<b>11. References</b>	<b>18</b>
<b>List of Symbols, Abbreviations, and Acronyms</b>	<b>20</b>
<b>Distribution List</b>	<b>21</b>

## List of Figures

Fig. 1	HMA showing the four independently controlled canards near the projectile nose .....	2
Fig. 2	E-flite EFLRDS76T off-the-shelf servo used in the HMA CAS.....	3
Fig. 3	CAS showing the servo actuating the canard blade.....	3
Fig. 4	Plot of $C_m$ vs. total angle of attack and canard deflection angle, $\alpha_c$ and canard deflection angle, $\delta$ showing the regions of attached, partially separated, and fully separated flow .....	5
Fig. 5	Mach number vs. time for the simulated flight.....	6
Fig. 6	Canard deflection angles and body angle of attack in each canard reference frame for the simulated flight.....	6
Fig. 7	Canard aerodynamic hinge moment over the flight.....	7
Fig. 8	Actuator test fixture to measure the dynamic response and steady-state deflection errors under varying hinge loads.....	8
Fig. 9	Plot of hinge load vs. $\delta$ for three spring configurations, along with the aerodynamic hinge moment vs. $\delta$ , $\alpha_c$ for Mach 0.6, 0.5, and 0.4 .....	9
Fig. 10	Actuator rise time vs. canard deflection command for each hinge load experiment. Average times are indicated, along with the 95th percentile rise time.....	10
Fig. 11	Actuator settling time vs. canard deflection command for each hinge load experiment. Average times are indicated, along with the 95th percentile settling time.....	11
Fig. 12	Actuator response to $10^\circ$ step commands, showing servo potentiometer output and encoder measurements of true canard position.....	12
Fig. 13	Measured canard aeroelasticity vs. hinge moment. The three spring configurations are identified, and a third-order polynomial fit to the data is plotted. ....	13
Fig. 14	Block diagram of flight simulation, showing the integration of the canard aerodynamic hinge moment model and the aeroelasticity model.....	14
Fig. 15	Mach number vs. time for the MC runset.....	14
Fig. 16	Canard deflection angles and body angle of attack in each canard reference frame for the MC runset.....	15
Fig. 17	Canard aerodynamic hinge moment over time for the MC runset.....	15
Fig. 18	CDF of the canard aerodynamic hinge moment in the coupled flight simulation over the entire MC runset, showing 95% of hinge loads below 0.57 Ncm.....	16
Fig. 19	Canard aeroelastic deflection over time for the MC runset.....	16

Fig. 20	CDF of the aeroelastic canard deflection in the coupled flight simulation over the entire MC runset, showing 95% of deflection offsets below $0.3^\circ$ .....	17
---------	--	----

## List of Tables

---



---

Table 1	Measured rise times and settling times .....	11
---------	--	----

## 1. Introduction

---

The Army's modernization priority of long-range precision fires is motivating research into maneuvering munition technologies to provide range extension of gun-launched munitions through trajectory shaping as well as terminal maneuver authority to engage imprecisely located, moving, and protected targets with precision. Improving munition maneuverability is a multidisciplinary effort influenced by a variety of factors. This study is focused on understanding the actuator dynamics to develop canard control technologies for subsonic flight regimes.

A key challenge to developing actuation technologies for the gun-launched environment is the high-g loads imparted to electromechanical components during the gun-launch event.<sup>1</sup> Additionally, the flight velocities and flight dynamics characteristics typically result in actuator performance requirements that demand a fast, precise response while overcoming the aerodynamic loads.

Cost is a significant constraint as well. The control actuation system is typically a significant driver of guided munition cost, and more-expensive munitions are purchased in smaller quantities and employed more sparingly. Prioritizing low-cost control actuation technologies helps preserve the high-volume fire capabilities typical of gun-based weapon systems, while improving the range and terminal control authority maneuverability of the munition.

Currently fielded gun-launched guided munitions make use of tactical missile or aerospace actuator technologies and harden them for the high-g gun launch.<sup>2,3</sup> These high-performance actuators provide desired maneuverability, but they are expensive. Recent research has successfully demonstrated an underactuated solution that uses fewer actuators to reduce cost by dithering a canard in phase with the projectile spin.<sup>4-7</sup> However, this inherent modulation of the control surface means this approach is better suited to small course corrections and is not well suited to high-maneuverability applications. Other maneuverability research has pursued the generation of asymmetric aerodynamic forces on the projectile body by injecting pulsed jets<sup>8</sup> or plasma into the flow,<sup>9</sup> or by modulating protrusions to create desirable shock interactions on fixed fins.<sup>10,11</sup> These approaches are survivable to high-g loads, but offer limited maneuverability and are only effective across limited flight regimes. Another approach uses piezoelectric actuators to morph an airfoil.<sup>12</sup> This concept is also well suited to high-g launch survivability, but offers only limited maneuverability due to the power requirements of piezoelectric actuation over large deflections.



The overarching goal of this research is to realize low-cost, fast-responding, high-g-tolerant control actuation technologies for guided munitions. Specifically, this research seeks to adapt low-cost, commercial off-the-self (COTS) technology into a high-g-survivable actuator. This report describes efforts to understand the effect of aerodynamic forces on the actuator dynamics and steady-state behavior under flight loads.

This report is organized as follows: An overview of the airframe and control concept is outlined in Section 2, and an actuator dynamic model is presented in Section 3 along with a model for the canard aerodynamics in Section 4. Expected canard deflection demands and overall flight characteristics are generated using flight simulation and are summarized in Section 5. The in-flight canard deflections are combined with the aerodynamic model to inform the design of a benchtop experiment (described in Section 6) that measures the effect of the canard aerodynamic hinge moment on the actuator dynamic and steady-state response. The actuator dynamic response is presented in Section 7, and the steady-state actuator behavior is presented in Section 8 and used to develop a model for the static canard aeroelasticity. Finally, in Section 9, the flight simulation is augmented to include the canard aerodynamic model and the aeroelasticity model, and demonstrates the actuator design is sufficient to provide the required control during flight.

## 2. Airframe and Control Actuation

---

Figure 1 illustrates a high-maneuverability airframe (HMA) used for technology demonstration purposes. The munition is 83 mm in diameter, 420 mm long, weighs about 3.3 kg, and flies in the subsonic regime after experiencing up to 10,000 g's of acceleration during gun launch. The vehicle features eight fixed fins in the rear for stabilization and four moveable canards toward the nose for control.<sup>13</sup>

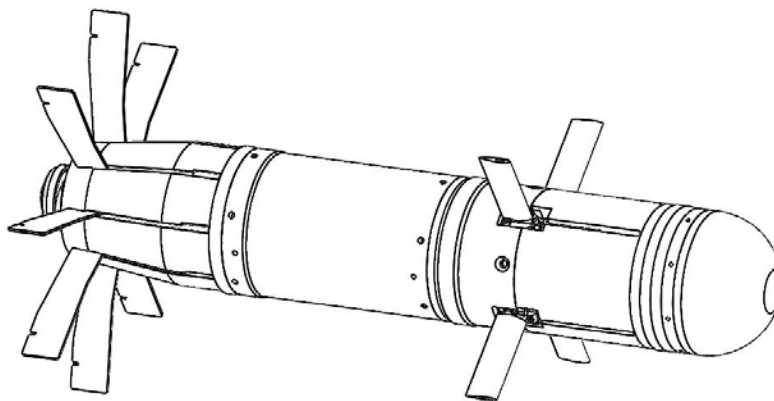


**Fig. 1** HMA showing the four independently controlled canards near the projectile nose

Canards are independently deflected with a  $\pm 10^\circ$  range through a control actuation system (CAS). The canards are actuated through a rigid bar linkage using an E-flite EFLRDS76T servomotor (hereafter referred to as servo), which has been modified by removing the stock electronic control circuitry. A digital signal processor (DSP) runs a custom controller to actuate all four canards to deflection angles provided by a flight control algorithm using the stock servo motors, gear train, and output shaft potentiometer.<sup>14,15</sup> Figure 2 shows the EFLRDS76T stock servo, and Fig. 3 shows the servomotor integrated into the assembly, actuating the canard through the linkage.



**Fig. 2** E-flite EFLRDS76T off-the-shelf servo used in the HMA CAS

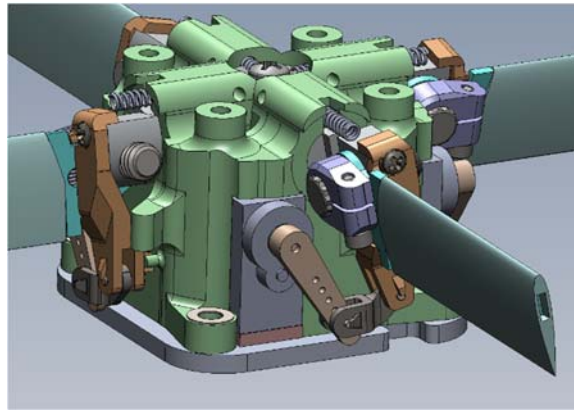


**Fig. 3** CAS showing the servo actuating the canard blade

### 3. Actuator Dynamic Model

---

The actuator dynamic behavior can be approximated with a linear, lumped-parameter dynamic model:

$$\ddot{\delta} + 2\zeta\omega_n\dot{\delta} + \omega_n^2(\delta - \delta_c) = 0, \quad (1)$$

where  $\delta$ ,  $\dot{\delta}$ , and  $\ddot{\delta}$  are the actuator deflection angle, angular velocity, and angular acceleration;  $\delta_c$  is the commanded canard deflection; and  $\zeta$ ,  $\omega_n$  are the damping ratio and system natural frequency. From these model parameters, actuator response metrics of rise time,  $T_r$ , and settling time,  $T_s$ , can be calculated:

$$T_r = \frac{2.23\zeta^2 - 0.078\zeta + 1.12}{\omega_n}. \quad (2)$$

$$T_s = \frac{4}{\zeta\omega_n} \quad \text{for } \zeta^2 \ll 1. \quad (3)$$

The static canard aeroelasticity is modeled as a deflection bias that perturbs the true deflection angle based on the canard aerodynamic hinge moment,  $M_{Hinge}$ , as shown in Eq. 4, where  $\hat{\delta}$  is the perturbed deflection angle, and  $\delta_{AE}(M_{Hinge})$  is the deflection bias due to the static aeroelasticity of the actuator.

$$\hat{\delta} = \delta + \delta_{AE}(M_{Hinge}). \quad (4)$$

#### 4. Canard Aerodynamic Model

---

Previous research developed a model for the canard aerodynamic hinge load as a function of both canard deflection angle,  $\delta$ , and the total canard angle of attack,  $\alpha_c$ , which is defined as the sum of  $\delta$  and the body attack angle in the plane perpendicular to the canard rotation axis,  $\alpha_\perp$ , as shown in the following equation<sup>16</sup>:

$$\alpha_c = (\alpha_\perp + \delta). \quad (5)$$

This model includes both  $\delta$  and  $\alpha_\perp$  contributions to  $C_m$ , allowing modeling of some of the secondary interaction effects; however, it does not account for the effect of the remaining body attack angle components parallel to the canard rotation axis. Although a more complete aerodynamic model would account for the effects of all body attack angle components, this model is sufficient to develop actuator hinge load estimates in this research.

The model for the canard aerodynamic hinge moment comprises a set of piecewise third-order polynomials in the form

$$C_m(\delta) = C_{m0}(\delta) + C_{m\alpha_c}(\delta) \sin(\alpha_c) + C_{m\alpha_c^3}(\delta) \sin^3(\alpha_c) \quad (6)$$

for canard deflection angle  $\delta$ , and total canard angle of attack,  $\alpha_c$  both in radians. The regions of attached flow, partial separation, and separated flow are each expressed as separate polynomials in the model, with a separate set of  $C_{m0}$ ,  $C_{m\alpha_c}$ ,  $C_{m\alpha_c^3}$  coefficients. The canard aerodynamic model is developed using an

aerodynamic reference diameter of 0.083 m, with a moment reference center of 0.1384 m, measured from the projectile nose. The underlying data were collected at Mach 0.175, at a Reynold's number of  $3.137 \times 10^5$ . Figure 4 plots the contour of the  $C_m(\delta)$  model as a function of body attack angle and canard deflection.

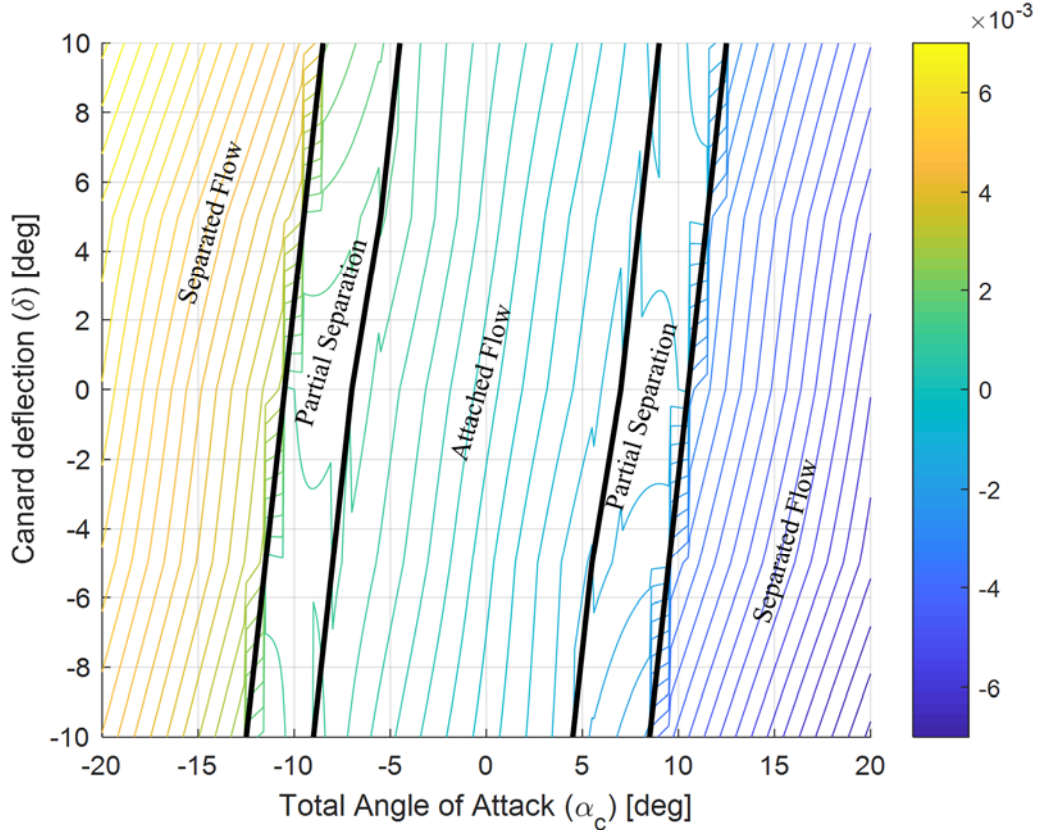


**Fig. 4** Plot of  $C_m$  vs. total angle of attack and canard deflection angle,  $\alpha_c$  and canard deflection angle,  $\delta$  showing the regions of attached, partially separated, and fully separated flow

## 5. Flight Conditions

A 6-degree of freedom (DOF) flight simulation is employed to determine the expected canard deflection demands during nominal flight. During the simulation, the flight controller and actuator model deflect the canards to guide the projectile to intercept a moving target, nominally located 850 m downrange with a 5-m/s cross-range velocity. Details of a representative munition flight are presented in Figs. 5 and 6.

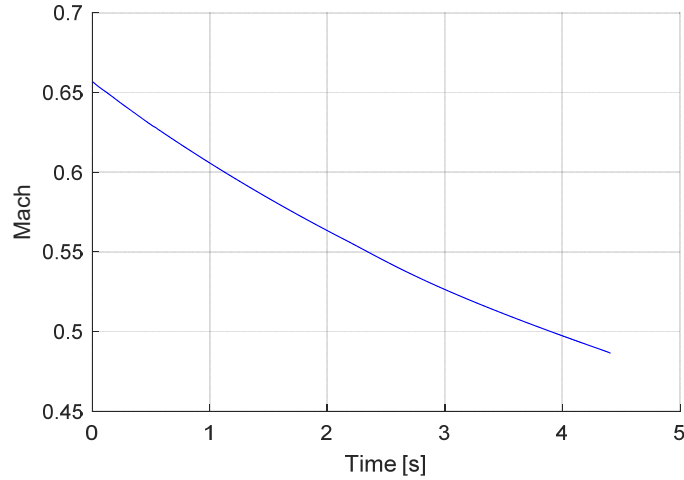


**Fig. 5 Mach number vs. time for the simulated flight**

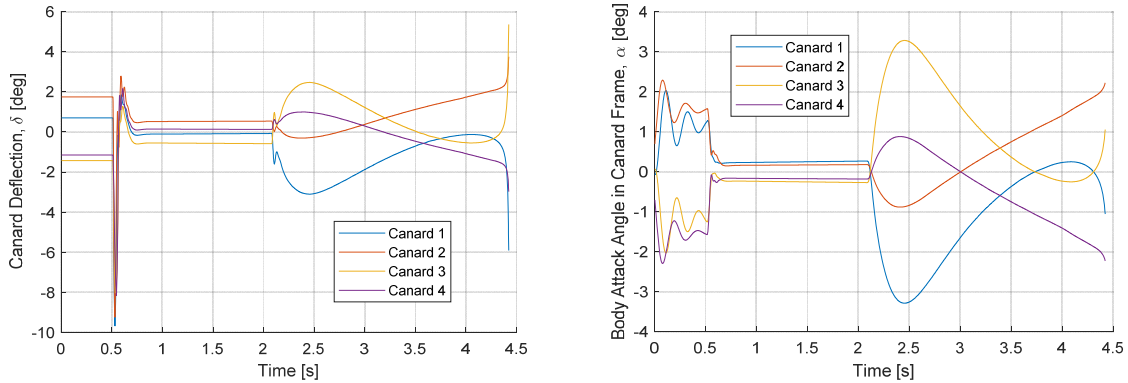


**Fig. 6 Canard deflection angles and body angle of attack in each canard reference frame for the simulated flight**

The launch velocity is Mach 0.66, and decays to Mach 0.48 over the 4.5-s flight, as shown in Fig. 5. Figure 6 plots the deflection angles for each canard, along with the body attack angle in each canard coordinate frame. As shown in Fig. 6, the flight controller damps the oscillations in angular motion from launch at around 0.5 s, and then begins intercept maneuvers at about 2 s, which last until impact at about 4.5 s. The deflection and attack angles presented here are typical for this munition, with canard deflections ranging from  $-10^\circ$  to  $10^\circ$  and body attack angles generally within  $\pm 4^\circ$ .

Using the  $C_m(\delta)$  model, the aerodynamic hinge moment on each canard hinge is calculated and presented in Fig. 7, using the atmospheric parameters, airspeed, canard deflection angles, and body attack angles from the flight simulation.

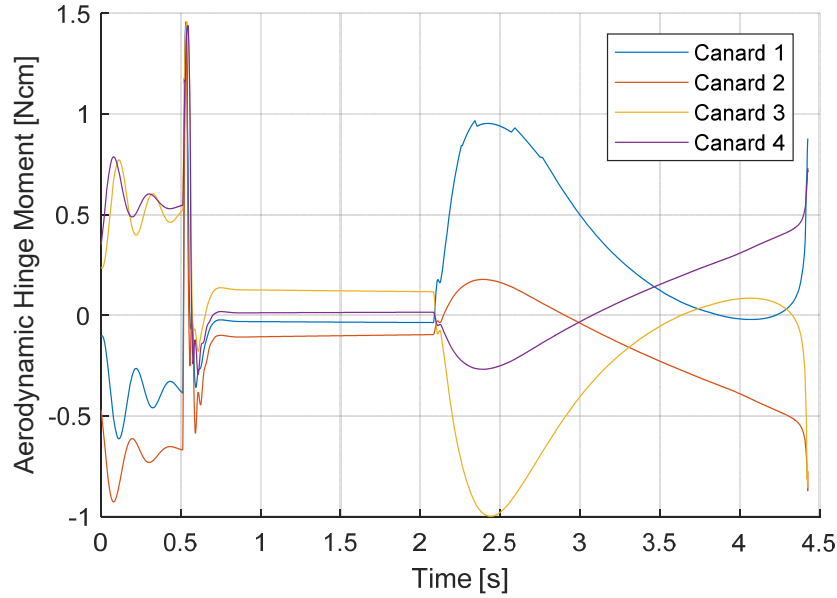
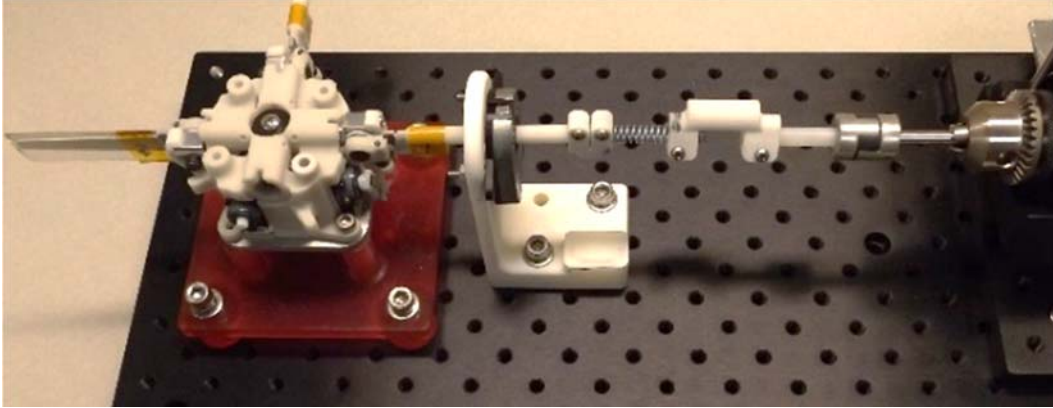


Fig. 7 Canard aerodynamic hinge moment over the flight

## 6. Experimental Apparatus

A benchtop actuator experiment was performed to measure the dynamic response of the actuator under representative flight loads and to quantify the steady-state errors in canard position. Figure 8 illustrates the apparatus, showing the CAS module with a surrogate canard blade equipped with a through-shaft encoder and fixed to a spring attached to a torque sensor. The CAS typically functions with the servo output potentiometer providing position feedback; however, in this experiment, canard deflection is measured both at the servo potentiometer and at the encoder on the canard, enabling measurement of the true canard deflection as well as the deformation of the canard drive linkage under load. The CAS DSP runs the motor controller driving the servo and records the canard position as measured through the servo potentiometer and canard blade encoder at 1 kHz, enabling investigation of the actuator dynamic response under load.



**Fig. 8 Actuator test fixture to measure the dynamic response and steady-state deflection errors under varying hinge loads**

A spring is used in the fixture to simulate the aerodynamic hinge moments experienced by the canard blade during flight. The spring in the fixture provides a torque-resisting canard deflection away from  $0^\circ$ , which grows linearly with deflection. The spring is designed to be variable length to scale the load applied to the canard.

Using the canard  $C_m(\delta)$  model from Eq. 6, the canard aerodynamic hinge moment calculated for Mach 0.6, 0.5, and 0.4, for  $\alpha_c$  ranging from  $-14^\circ$  to  $14^\circ$  while  $\delta$  ranges from  $-10^\circ$  to  $10^\circ$ . These parameters are chosen to span the flight conditions from launch to impact in order to collect data across the operational spectrum. Figure 9 plots the aerodynamic hinge moment versus  $\delta, \alpha_c$  for these Mach numbers. The test fixture spring is adjusted to three lengths that provide 3, 2, and 1 Ncm at  $\pm 10^\circ$  deflection. These 3-, 2-, and 1-Ncm spring configurations model the aerodynamic hinge moment at Mach 0.6, 0.5, and 0.4, respectively, as shown in Fig. 9.

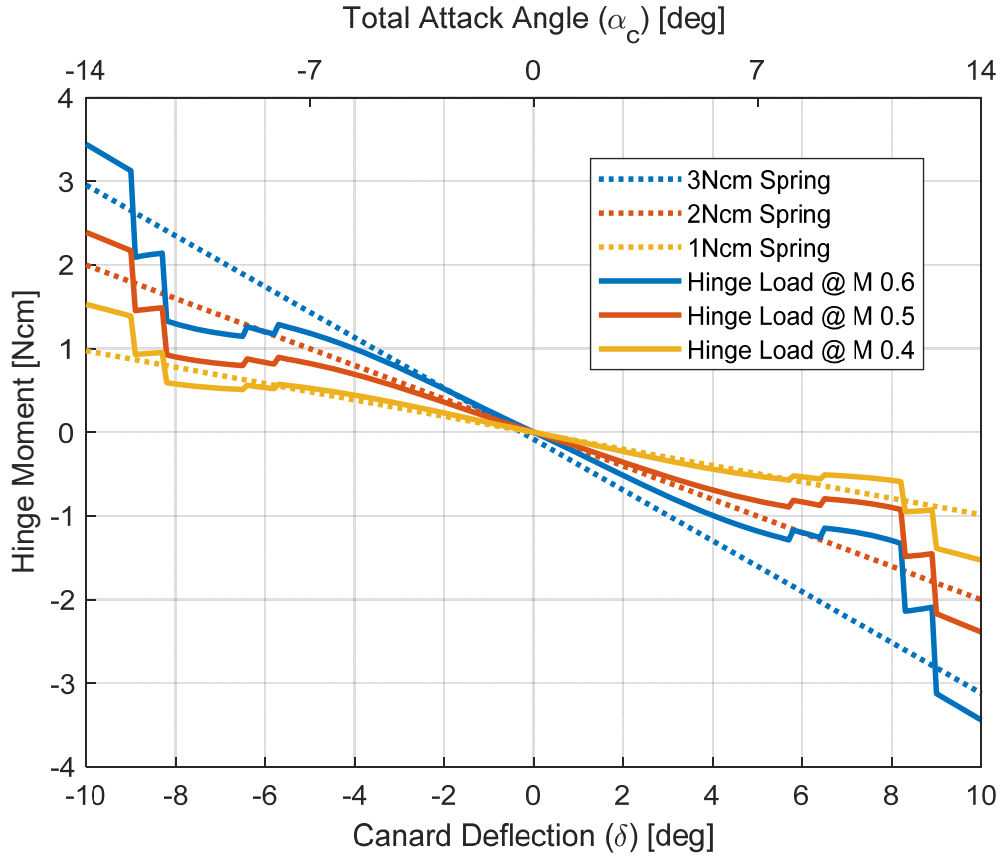


**Fig. 9** Plot of hinge load vs.  $\delta$  for three spring configurations, along with the aerodynamic hinge moment vs.  $\delta$ ,  $\alpha_c$  for Mach 0.6, 0.5, and 0.4

## 7. Actuator Dynamic Response

Deflection step commands are supplied to the CAS DSP under the different spring configurations, while the actuator response is recorded. In this series of experiments, step response data are collected for positive and negative direction steps spanning the  $\pm 10^\circ$  actuator range of motion for each of the spring configurations modeling Mach 0.6, 0.5, and 0.4 hinge moments.

The rise time for the actuator is calculated from the position response from each dataset and is plotted in Fig. 10. The data show similar actuator response across the range of canard hinge loads and deflection commands. The average rise time at each hinge load for all deflection commands is shown, as well as the grand average rise time of 0.00847 s for all data collected. From this data, a 95th percentile rise time of 0.01067 s is identified to provide a conservative estimate of actuator performance across the experiment conditions.



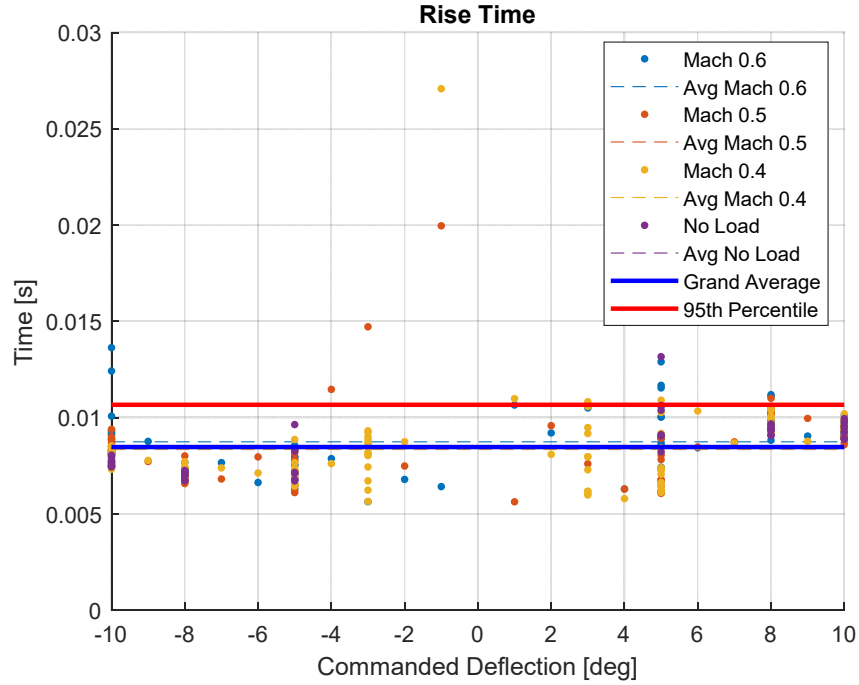


**Fig. 10** Actuator rise time vs. canard deflection command for each hinge load experiment. Average times are indicated, along with the 95th percentile rise time.

The actuator settling time is also calculated from the position response collected in each dataset and is plotted in Fig. 11. The data show more variability than the rise time analysis, but the actuator settling time across the range of canard hinge loads and deflection commands remains consistent. The average settling time at each hinge load for all deflection commands is shown, as well as the grand average settling time of 0.0209 s for all data collected. From this data, a 95th percentile settling time of 0.0314 s is identified to provide a conservative estimate of actuator performance across the experiment conditions. Table 1 presents the average rise time and settling time for each of the spring configurations in this experiment, along with the overall average and 95th percentile times.

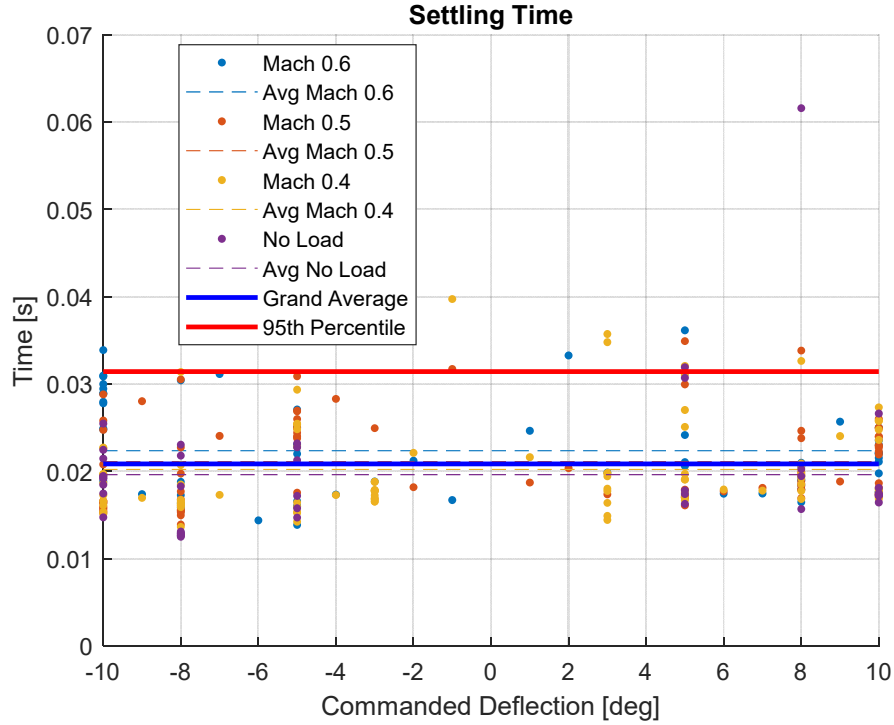


**Fig. 11** Actuator settling time vs. canard deflection command for each hinge load experiment. Average times are indicated, along with the 95th percentile settling time.

**Table 1** Measured rise times and settling times

Flight condition	Rise time, $T_r$ (s)	Settling time, $T_s$ (s)
Mach 0.6	0.00874	0.0224
Mach 0.5	0.00842	0.0211
Mach 0.4	0.00834	0.0202
No load	0.00840	0.0196
Grand average	0.00847	0.0209
95th percentile	0.01067	0.0314

From Eqs. 2 and 3, the  $T_r$  and  $T_s$  for the 95th percentile can be used to determine a corresponding  $\zeta$ ,  $\omega_n$  to populate the actuator dynamic model. A  $T_r$  of 0.01067 s and  $T_s$  of 0.0314 s correspond to  $\zeta$  of 0.66 and  $\omega_n$  of 193 rad/s.

## 8. Actuator Static Aeroelasticity

The measured actuator step response data are also analyzed to characterize the steady-state deformation of the canard drive linkage from the servo to the blade while under different hinge loads. Example response data for 10 step responses

from  $0^\circ$  to  $10^\circ$  are plotted in Fig. 12 , for the actuator with no spring load and with the spring configured to emulate aerodynamic loads at Mach 0.4, 0.5, and 0.6. The actuator linear quadratic integral controller compensates for the external hinge moment and drives the servo to the required position; however, the controller only has access to feedback from the servo output shaft potentiometer, not true canard deflection. The increasing aerodynamic hinge moment applied to the canard results in deformation of the linkage between the servo and canard blade, as shown by the separation between the encoder recorded position and the position indicated by the servo potentiometer.

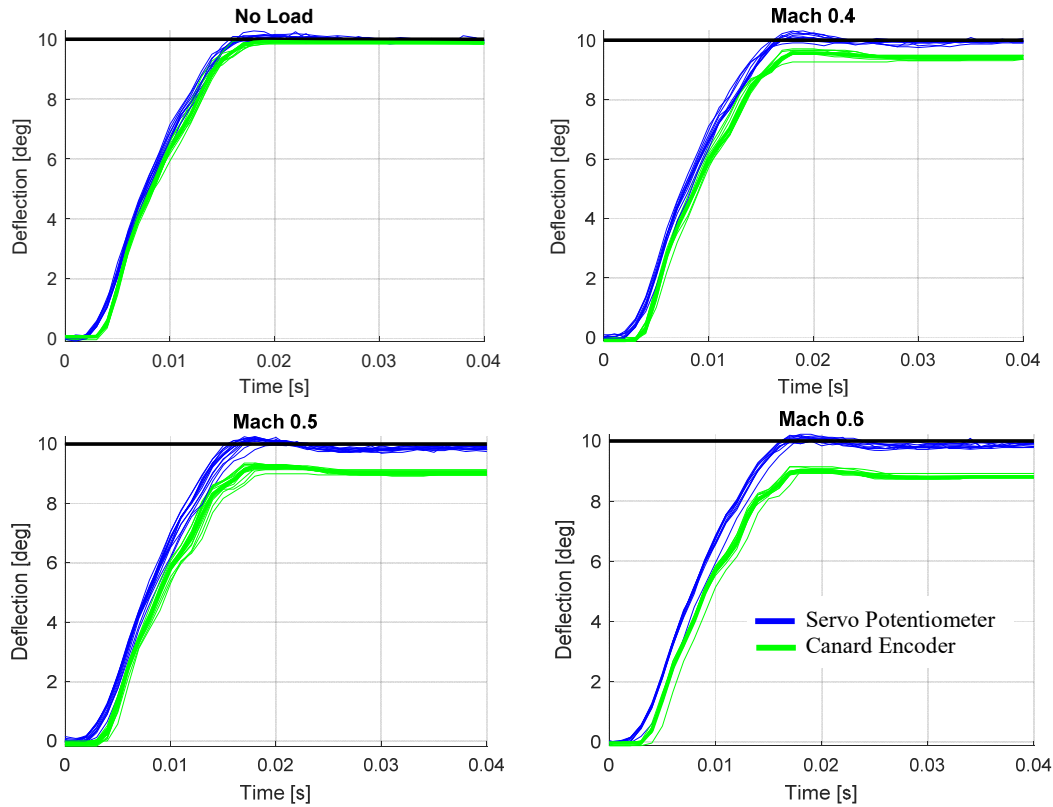


**Fig. 12 Actuator response to  $10^\circ$  step commands, showing servo potentiometer output and encoder measurements of true canard position**

The steady-state difference between the encoder measurement of canard position and the commanded deflection is the aeroelastic deformation of the canard,  $\delta_{AE}$ . The step commands of varying magnitudes were analyzed for all three spring configurations to calculate the steady-state  $\delta_{AE}$ , along with the canard hinge moment from the spring. These  $\delta_{AE}$  versus hinge moment measurements are plotted in Fig. 13.

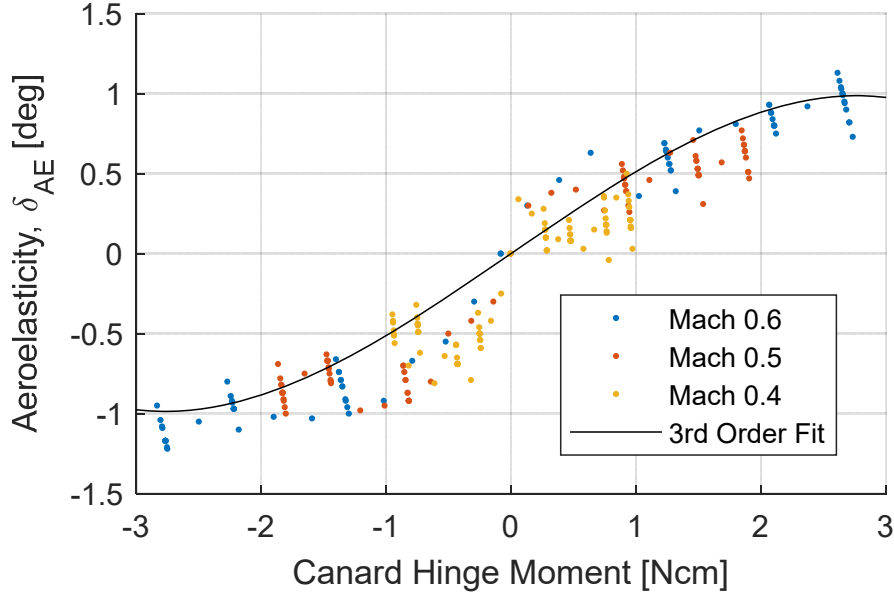


**Fig. 13** Measured canard aeroelasticity vs. hinge moment. The three spring configurations are identified, and a third-order polynomial fit to the data is plotted.

A model of static canard aeroelasticity is created by regressing a third-order polynomial to the experiment data:

$$\delta_{AE} = -0.023356 * (M_{Hinge})^3 + 0.53541 * M_{Hinge}, \quad (7)$$

where canard hinge moment,  $M_{Hinge}$ , is in units of newton centimeters, and canard aeroelasticity,  $\delta_{AE}$  is in units of degrees.

## 9. Coupled Flight Simulation Analysis

The actuator model within the 6-DOF flight simulation is the linear, lumped-parameter dynamic model presented in Eq. 1. The flight simulation actuator model is updated with the 95th percentile dynamic model parameters,  $\zeta = 0.66$  and  $\omega_n = 193$ , corresponding to the conservative estimate of actuator dynamic response. Additionally, the aerodynamic hinge moment model,  $C_m(\delta)$ , from Eq. 6, and the canard aeroelasticity model,  $\delta_{AE}(M_{Hinge})$ , from Eqs. 4 and 7 are integrated into the simulation. Figure 14 shows a block diagram of the integration of the canard aerodynamic hinge moment model and aeroelasticity model into the actuator and flight dynamics models. The  $\delta_{AE}$  is calculated and added to the canard deflection angle from the actuator dynamic model to create a modified deflection,  $\hat{\delta}$ , feeding into the flight dynamics model. These enhancements enable the canard hinge moment to be calculated from the body attack angles and canard

deflections and the resulting canard aeroelastic deformation to be imposed in the simulation.

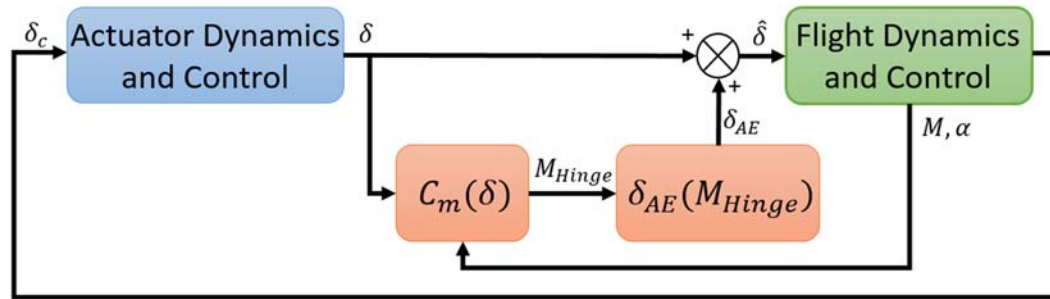


**Fig. 14** Block diagram of flight simulation, showing the integration of the canard aerodynamic hinge moment model and the aeroelasticity model

A set of 100 flights are modeled using the upgraded flight simulation with Monte Carlo (MC) errors to add uncertainty in parameters such as the initial conditions and sensor errors in-flight.<sup>13</sup> Flight details are presented in Figs. 15 and 16. The launch velocity is generally between Mach 0.625 and Mach 0.7, and decays to Mach 0.5–0.45 over the flight. The canard deflection angles range from  $-10^\circ$  to  $10^\circ$  and body attack angles generally within  $\pm 4^\circ$ .

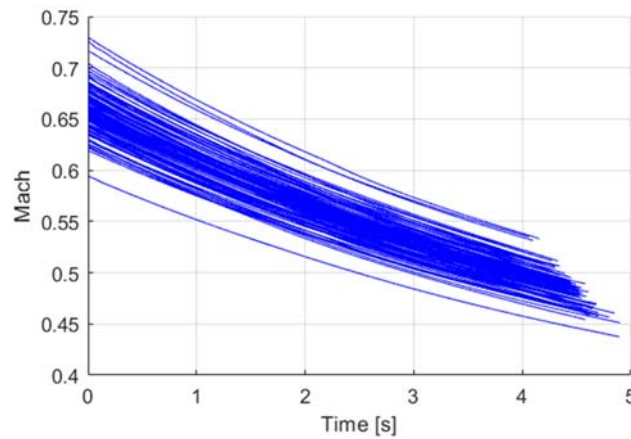


**Fig. 15** Mach number vs. time for the MC runset

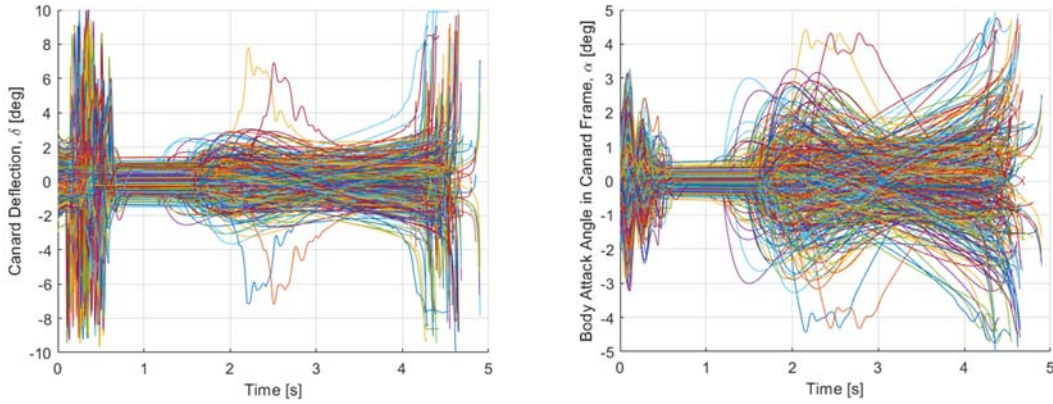


**Fig. 16** Canard deflection angles and body angle of attack in each canard reference frame for the MC runset

Using the integrated  $C_m(\delta)$  model, the aerodynamic hinge moment on each canard is calculated at each timestep during the simulation, as shown in Fig. 17. A cumulative density function (CDF) is created from the data and plotted in Fig. 18, showing a 95th percentile hinge moment of 0.57 Ncm across all flights.

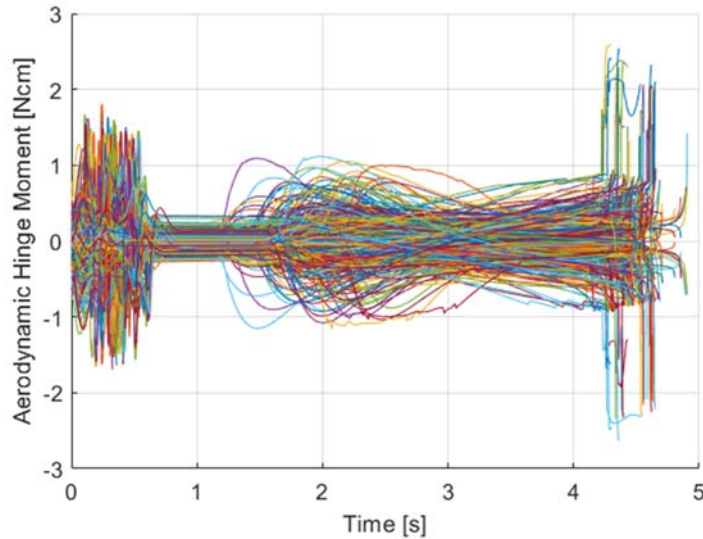


**Fig. 17** Canard aerodynamic hinge moment over time for the MC runset

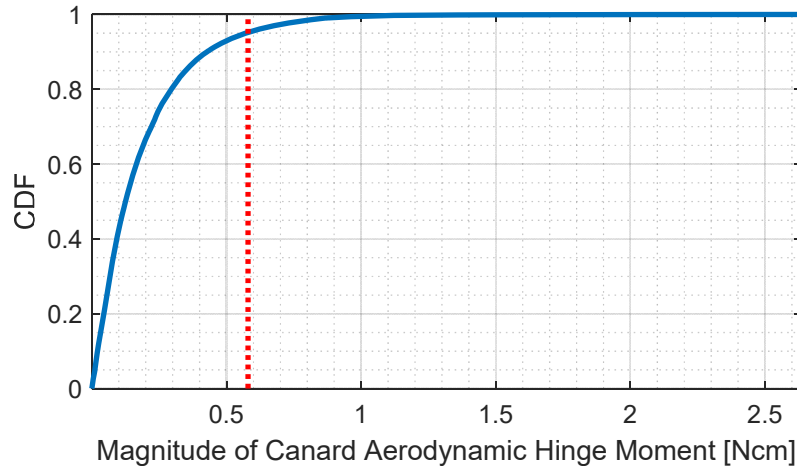


**Fig. 18** CDF of the canard aerodynamic hinge moment in the coupled flight simulation over the entire MC runset, showing 95% of hinge loads below 0.57 Ncm

Using the integrated  $\delta_{AE}(M_{Hinge})$  model, the aeroelastic deformation of each canard is calculated at each timestep during the simulation, as shown in Fig. 19. A CDF is created from the data and plotted in Fig. 20, showing a 95th percentile aeroelastic deflection of  $0.3^\circ$ .

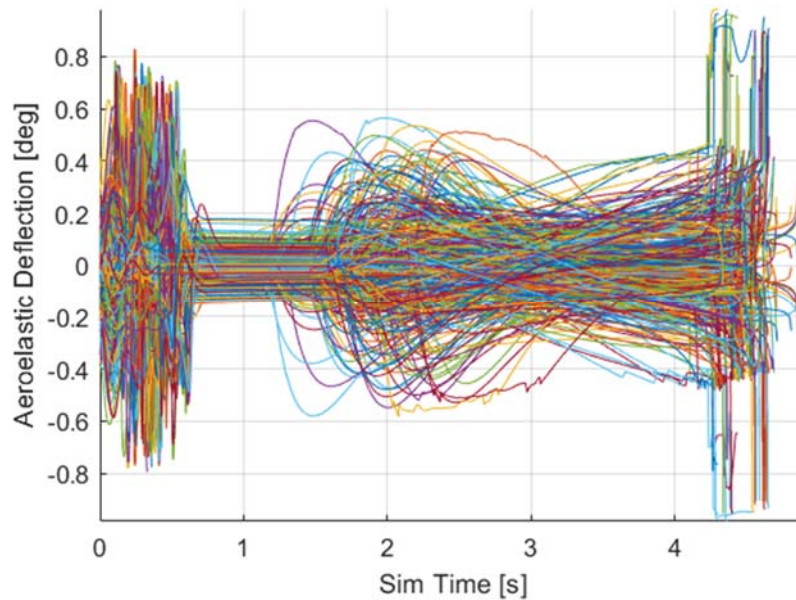


**Fig. 19** Canard aeroelastic deflection over time for the MC runset

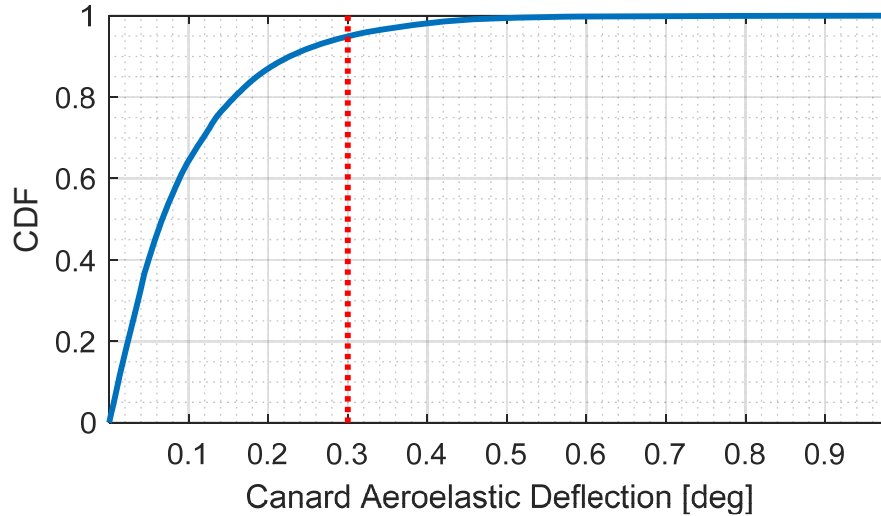


**Fig. 20 CDF of the aeroelastic canard deflection in the coupled flight simulation over the entire MC runset, showing 95% of deflection offsets below 0.3°**

The 100 MC flights were simulated again using the original flight simulation with the same random number seeds in order to evaluate the effect of the canard aeroelasticity on the munition performance. The flight simulation with the coupled canard aerodynamics simulation produced 50% circular error probable (CEP) of 0.091 m over the 100 MC flights, while the original simulation returned a 50% CEP of 0.101 m. This small difference of 0.01 m between the simulation sets indicates the flight controller is able to overcome the canard aeroelasticity and maintain overall system performance.

## 10. Conclusion

The overall objective of this research is to realize low-cost, fast-responding, high-g-tolerant control actuation technologies for guided munitions. This work contributes to that goal by focusing on understanding the effect of aerodynamics on actuator aeroelasticity and dynamics as well as the flight dynamics.

A flight simulation was used to characterize the expected canard deflection demands and overall flight conditions, which informed the design of a benchtop actuator experiment to measure the effect of canard aerodynamic hinge moment on the actuator dynamic and steady-state response. The steady-state behavior of the actuator under varying canard hinge moments was used to develop a model for the static canard aeroelasticity, and the flight simulation was augmented to include both the canard aerodynamic model and the aeroelasticity model. The improved flight simulation was used to demonstrate the low-cost, semi-COTS actuator design is sufficient to provide the required control during flight.



## 11. References

---

1. Carlucci DE, Frydman AM, Cordes JA. Mathematical description of projectile shot exit dynamics (set forward). *Journal of Applied Mechanics*. 2013;80:031501-1–9.
2. Bender JM. Structural analysis of the Excalibur canard actuation system and the guidance and navigation unit. Aberdeen Proving Ground (MD): Army Research Laboratory (US); 2008 Apr. Report No.: ARL-TR-4412.
3. General Dynamics Ordnance and Tactical Systems. Missile Components. Control Actuator Systems (CAS). St Petersburg (FL): General Dynamics; c1995–2018 [accessed 2018 Aug 24]. [https://www.gd-ots.com/missiles-and-rockets/missile-components/control\\_actuator\\_systems/](https://www.gd-ots.com/missiles-and-rockets/missile-components/control_actuator_systems/).
4. Fresconi FE, Harkins T. Experimental flight characterization of asymmetric and maneuvering projectiles from elevated gun firings. *Journal of Spacecraft and Rockets*. 2012;49(6):1120–1130.
5. Fresconi FE. Guidance and control of a projectile with reduced sensor and actuator requirements. *Journal of Guidance, Control, and Dynamics*. 2011;34(6):1757–1766.
6. Fresconi FE, Brown G, Celmins I, DeSpirito J, Ilg M, Maley J, Magnotti P, Scanlan A, Stout C, Vazquez E. Very affordable precision projectile technology development and flight demonstrations. Aberdeen Proving Ground (MD): Army Research Laboratory (US); 2011 Feb. Report No.: ARL-TR-5460.
7. Fairfax L, Fresconi F, Maley J, inventors; US Secretary of the Army, assignee. Method and apparatus for GPS-denied navigation of spin-stabilized projectiles. United States patent US 9,702,674. 2017 July 11.
8. McMichael J, Lovas A, Plostins P, Sahu J, Brown G, Glezer A. Microadaptive flow control applied to a spinning projectile. Aberdeen Proving Ground (MD): Army Research Laboratory (US); 2005 Sep. Report No.: ARL-TR-3589.
9. Gnemmi P, Rey C. Plasma actuation for the control of a supersonic projectile. *Journal of Spacecraft and Rockets*. 2009;46(5):989–998.
10. Kim D, Strickland L, Gross M, Rogers J, Costello M, Fresconi F, Celmins I. Actuator design and flight testing of an active microspoiler-equipped projectile. *ASME J Dyn Sys Meas Control*. 2017;139(11):111002-111002-15. doi:10.1115/1.4036808.

11. Celmins I. Design and evaluation of an electromechanical actuator for projectile guidance. Aberdeen Proving Ground (MD): Army Research Laboratory (US); 2007 Sep. Report No.: ARL-MR-0672.
12. Weinacht P. Coupled CFD/GN&C modeling for a smart material canard actuator. Aberdeen Proving Ground (MD): Army Research Laboratory (US); 2007 Sep. Report No.: ARL-TR-4265.
13. Fresconi FE, Celmins I, Sifton S, Costello M. High maneuverability projectile flight using low cost components. *Aerospace Science and Technology*. 2015;41:175–188.
14. Burchett B. Matlab tools for automated system identification and control design of single-input single-output (SISO) motor loops. Aberdeen Proving Ground (MD): Army Research Laboratory (US); 2017 July. Report No.: ARL-CR-0817.
15. Bryson J, Fresconi F. Low-cost actuator dynamic model and controller development for gun-launched munitions. Aberdeen Proving Ground (MD): Army Research Laboratory (US); 2018 Aug. Report No.: ARL-TR-8471.
16. Bryson J, Celmins, I., Fresconi F. Aerodynamic model for canard control actuation on a subsonic, gun-launched munition. Aberdeen Proving Ground (MD): Army Research Laboratory (US); 2018 Sep. Report No.: ARL-TR-8496.

## List of Symbols, Abbreviations, and Acronyms

---

CAS	control actuation system
CDF	cumulative density function
CEP	circular error probable
COTS	commercial off-the-self
DOF	degree of freedom
DSP	digital signal processor
HMA	high-maneuverability airframe
MC	Monte Carlo

1 DEFENSE TECHNICAL  
(PDF) INFORMATION CTR  
DTIC OCA

2 DIR ARL  
(PDF) IMAL HRA  
RECORDS MGMT  
RDRL DCL  
TECH LIB

1 GOVT PRINTG OFC  
(PDF) A MALHOTRA

1 ARL  
(PDF) RDRL WML E  
J BRYSON